Physics of Fluids

RESEARCH ARTICLE | NOVEMBER 18 2026

Unsteady airwake dynamics of generic destroyer: A spectral and wavelet approach

Ali Dogrul (Doğrul) ; Sarih Sari (Sarı) ; Muhammet Taha Akkoc (Akkoç) ; Seyfettin Bayraktar

Check for updates

Physics of Fluids 38, 115141 (2026)
https://doi.org/10.1063/5.0358047

View Online Export Citation

Articles You May Be Interested In

Unsteady carrier airwake under complex sea states flow characteristics and time-conditioned prediction
Physics of Fluids (September 2026)

Large eddy simulation of ship airflow control with steady Coanda effect
Physics of Fluids (January 2023)

Application of a non-equilibrium wall model with convective term modeling in complex separated flows
Physics of Fluids (May 2026)

18 November 2026 10:48:16

AIP Publishing
Physics of Fluids
Special Topics Open for Submissions
Learn More

AIP Publishing

Physics of Fluids ARTICLE pubs.aip.org/aip/pof

Unsteady airwake dynamics of generic destroyer: A spectral and wavelet approach

Cite as: Phys. Fluids **38**, 115141 (2026); doi: 10.1063/5.0358047
Submitted: 26 August 2026 · Accepted: 4 November 2026 ·
Published Online: 18 November 2026

View Online Export Citation CrossMark

Ali Dogrul (Doğrul),[1,a)] Sarih Sari (Sarı),[2] Muhammet Taha Akkoc (Akkoç),[3] and Seyfettin Bayraktar[4]

AFFILIATIONS

[1]Department of Naval Architecture and Marine Engineering, National Defense University, Turkish Naval Academy, 34942 Istanbul, Turkey
[2]Department of Naval Architecture and Marine Engineering, Yildiz Technical University, 34349 Istanbul, Turkey
[3]Department of Mechanical Engineering, National Defense University, Turkish Naval Academy, 34942 Istanbul, Turkey
[4]Department of Marine Engineering, Yildiz Technical University, 34349 Istanbul, Turkey

[a)]Author to whom correspondence should be addressed: ali.dogrul@msu.edu.tr

ABSTRACT

The turbulent wake of naval ship geometries is important because the ship's superstructure is a blunt body. The investigation of the unsteady airwake behind the superstructure provides an in-depth investigation of time-series velocity data obtained by numerical analyses. This study focuses on spectral and wavelet analysis to determine the coherent structures in detail. Fast Fourier transform (FFT), power spectral density (PSD), and continuous wavelet transform (CWT) analyses were performed using in-house developed code. In the transition from the time domain to the frequency domain, the amplitude spectrum was derived using an FFT, and the CWT was also employed to show the intermittency of coherent structures and vortex shedding. The wavelet scalograms show the relationship between amplitude and time; in addition, turbulent kinetic energy (TKE) and turbulence intensity were calculated from the PSD data. The results reveal the sensitivity of the fluctuation velocity components and the TKE for broadband turbulence at different wind-over-deck angles. The signal processing of raw time-series data reveals details of flow in the ship airwake region, enabling comprehensive characterization of turbulence. The vertical-axis (w) vortex breaks are dominated by the resonant characteristics of the hangar geometry (backward-facing step), independent of the wind direction, while for the lateral-axis (v), asymmetric wind-over-deck angles result in a significant shift of spectral energy toward higher frequency bands.

Published under an exclusive license by AIP Publishing. https://doi.org/10.1063/5.0358047

18 November 2026 10:48:16

I. INTRODUCTION

The airwake behind the superstructure of naval vessels includes turbulent structures over the flight deck.

The flow around the superstructure, especially over the flight deck, must be considered in detail to ensure safe helicopter operating limits (SHOL). Many studies have been carried out using simple frigate forms (SFS1, SFS2), a modern benchmark ship (ONRT), and the latest and most realistic design, NATO-generic destroyer (NATO-GD). Most studies have focused on experimentally determining the flow field by conducting model tests in wind tunnels. Although several recent studies have focused on the ship airwake of various ship models, there remains a notable lack of detailed investigations concerning the distribution of turbulent kinetic energy (TKE) and turbulence intensity (TI) over the flight deck. While early research often focused on basic aerodynamic assessments, the literature can be broadly categorized into three thematic areas: experimental validation of airwake topologies, the evaluation of CFD scale effects and high-fidelity modeling, and dynamic interface investigations concerning ship-rotorcraft interactions.

Traditional wind tunnel testing remains a cornerstone of airwake prediction, providing physical validation for complex aerodynamic phenomena. Seth *et al.*[1] investigated unsteady flows over the SFS2 model using time-resolved particle image velocimetry (TR-PIV) in a low-speed wind tunnel. Their work demonstrated the influence of the atmospheric boundary layer (ABL) on large-scale unsteady flow separation and vorticity shedding from the superstructure. To standardize research methodologies, Owen *et al.*[2] and Fernandez *et al.*[3] introduced the NATO-GD benchmark, providing a consistent platform for evaluating ship-induced turbulence and its interaction with the atmospheric boundary layer. Using this framework, Chen and Rauleder[4] conducted a comprehensive stereoscopic PIV investigation on a 1:100-scale NATO-GD model, revealing that varying wind-over-deck (WOD)

Published under an exclusive license by AIP Publishing

angles cause significant spatial non-uniformities and localized velocity deficits, particularly near the hangar.

While wind tunnel tests are fundamental, they inherently face scaling challenges. Polsky[5] highlighted that computational fluid dynamics (CFD) mitigates these issues by enabling full-scale, time-accurate predictions, which are crucial for aircraft operational safety. The importance of scale was further underscored by Scott *et al.*,[6] who used CFD to show that larger ship sizes generate more turbulent wakes, significantly increasing pilot workload. Accurately capturing these transient structures requires advanced, turbulence-resolving solvers. Linton and Thornber[7] employed high-fidelity simulations on the SFS1 benchmark to show the high sensitivity of the flight deck aerodynamic environment to WOD conditions and spatial positioning. Similarly, Sari *et al.*[8] compared SST-k-omega and detached eddy simulation (DES) models for the NATO-GD, concluding that while RANS models capture general velocity fields, DES is essential for the detailed characterization of turbulence intensity. Exploring computational efficiency, Kurban *et al.*[9] compared high-fidelity URANS with mid-fidelity lattice Boltzmann method (LBM) simulations for the SFS2 model, finding that LBM accurately captured headwind flow structures at a reduced computational cost, despite some discrepancies at higher yaw angles.

The synthesis of experimental and numerical methods ultimately aims to optimize the ship-helicopter dynamic interface. Forrest *et al.*[10] established a definitive link between a vessel's superstructure geometry and resulting aerodynamic disturbances, demonstrating how discrete structural discontinuities on platforms like the Type 23 frigate dictate turbulence intensity and spatial instabilities. To translate these aerodynamic findings into operational safety, airwake models are increasingly integrated into flight simulators. Yuan *et al.*[11] used OpenFOAM to generate realistic airwake characteristics for the CPF vessel, while the subsequent SHOLAS project[12] integrated advanced CFD, high-fidelity wind tunnel tests, and full-scale sea trials to validate airwake simulations for industrial flight simulators. Wall *et al.*[13] further expanded on operational realism by investigating environmental factors, demonstrating that realistic ship motions directly transmit energy to the airwake, thereby altering its frequency spectrum and escalating pilot workload. Advancing the modeling of ship-rotorcraft interactions, Kurban *et al.*[14] used efficient LBM simulations to model the aerodynamic coupling between the NATO-GD and rotorcraft airwakes, proving that reduced-velocity sets can achieve accurate, cost-effective predictions for deck landing operations.

Despite these advancements, the current literature predominantly relies on time-averaged or purely power spectral density (PSD)-focused approaches, which do not fully capture the intermittent nature of the flow. While some studies on ship-rotor interaction have presented time-frequency analyses, no specific study on isolated ship airwakes using a combination of Fast Fourier transform (FFT), PSD, and continuous wavelet transform (CWT) methods to obtain the amplitude spectrum and perform time-frequency analysis was found. Therefore, this study not only presents highly resolved NATO-GD data but also, for the first time in the literature, demonstrates, using CWT, when and how large-scale coherent structures on the flight deck break down into high-frequency fluctuations.

In this study, the numerical setup validated in the authors' previous work[8] was used to conduct entirely new IDDES simulations. A comprehensive grid of 75 measurement points was established, and new time-series velocity data were extracted for various wind-over-deck (WOD) angles. The main purpose of the study is to show the effects of wind-over-deck (WOD) angle on the fast Fourier transform (FFT), power spectral density (PSD), and continuous wavelet transform (CWT) responses at various points over the flight deck. The numerical analyses from the authors' previous study[8] were revisited, and time-domain velocity components were obtained at various points over the flight deck. While the literature heavily relies on time-averaged flow topologies and basic spatial turbulence intensities, the highly intermittent nature of ship airwakes requires advanced time-frequency analysis. This study bridges this gap by applying signal processing methods like FFT, PSD, and CWT. Unlike the authors' previous study,[8] which was limited to the numerical validation of the IDDES model under headwind conditions, the present work introduces a novel spectral post-processing methodology on newly generated asymmetric WOD angle datasets. The numerical analyses were conducted for WOD angles between Red 30° and Green 30°. The observation points were located from starboard to port to show the effects of WOD angle across the flight deck. The time-domain velocity data were first converted to the frequency domain using an FFT to identify dominant flow periodicities, such as vortex-shedding frequencies originating from the superstructure. Then PSD graphs were obtained for each scenario to characterize the spectral energy distribution. The turbulent fluctuations were also calculated using the PSD data. Finally, CWT analyses were conducted to assess the correlation between shedding frequency and time-varying energy variance. The CWT scalogram shows not only the dominant frequency-dependent turbulence characteristics but also the exact temporal occurrence of this unsteady wake field. The amplitude spectrum and time-frequency analysis show more details on the turbulence characteristics of the ship airwake region over the flight deck.

II. THEORETICAL BACKGROUND

A. NATO-GD geometry

The latest benchmark design by the NATO AVT-315 Research Task Group has a realistic superstructure with a mast, funnel, and radar. The main dimensions and the detailed experimental data are presented since the wind tunnel tests were carried out on a 1/50 scale factor.[2] The details of the ship geometry are provided in Table I. The main dimensions are given in full and model scales. The coordinate system (x_2, y_2, z_2) used in the present study is located in the intersection of the hangar wall and the flight deck.

B. Governing equations and numerical setup

The numerical analyses were carried out using the Improved Delayed Detached Eddy Simulation (IDDES) turbulence modeling

TABLE I. Main particulars of the NATO-GD destroyer.

Parameter	Definition	Full	Model 1
λ	Scale	1	1/50
L_{WL} (m)	Length waterline	150	3
B_{WL} (m)	Beam waterline	16.8	0.336
Δ (ton[a]) − (kg)	Displacement	6167[a]	49.3

[a]in tons.

18 November 2026 10:48:16

Published under an exclusive license by AIP Publishing

method, employing the SST k–ω turbulence model. The governing equations are given below

$$\frac{\partial U_i}{\partial x_i} = 0, \tag{1}$$

$$\frac{\partial U_i}{\partial t} + U_j \frac{\partial U_i}{\partial x_j} = -\frac{1}{\rho}\frac{\partial P}{\partial x_i} + \frac{\partial}{\partial x_j}\left[\upsilon\left(\frac{\partial U_i}{\partial x_j} + \frac{\partial U_j}{\partial x_i}\right)\right] - \frac{\partial \overline{u_i' u_j'}}{\partial x_j}, \tag{2}$$

$$\frac{\partial \rho k}{\partial t} + \nabla(\rho \vec{U} k) = \nabla(\mu + \sigma_k \mu_t) + P_k - \rho\sqrt{k^3}/l_{IDDES}, \tag{3}$$

$$\frac{\partial \rho \omega}{\partial t} + \nabla(\rho \vec{U} \omega) = \nabla(\mu + \sigma_\omega \mu_t) + 2(1 - F_1)\rho\sigma_{\omega 2}\frac{\nabla k \nabla \omega}{\omega} + \alpha\frac{\rho}{\mu_t}P_k - \beta\rho\omega^2, \tag{4}$$

$$\mu_t = \rho\frac{a_1 \cdot k}{\max(a_1 \cdot \omega, F_2 \cdot S)}, \tag{5}$$

$$P_k = \min\left(\mu_t S^2, 10 \cdot C_\mu \rho k \omega\right). \tag{6}$$

In the above equations, F_1 and F_2 are the SST blending functions. The IDDES length scale is as follows

$$l_{IDDES} = \tilde{f}_d . l_{RANS} + \left(1 - \tilde{f}_d\right) \cdot l_{LES}, \tag{7}$$

$$l_{LES} = C_{DES}\Delta, \tag{8}$$

$$l_{RANS} = \frac{\sqrt{k}}{C_\mu \omega}, \tag{9}$$

$$C_{DES} = C_{DES1} \cdot F_1 + C_{DES2} \cdot (1 - F_1), \tag{10}$$

$$\Delta = \min\left\{C_\omega \max[d_\omega, h_{\max}], h_{\max}\right\}. \tag{11}$$

The IDDES is an improved, high-fidelity version of DDES. While DDES is generalized for separated flows, IDDES offers enhanced resolution for complex geometries. The details and comparison of these two models can be found in Refs. 15–18.

In the present study, the numerical setup is designed to mimic the wind tunnel experiments, neglecting free-surface effects, so the numerical analyses were performed in single-phase (air). The computational domain was designed as a circular domain, similar to that used in a recent study[19,20] for the numerical setup. The commercial CFD solver Siemens PLM Star CCM+ was used for the numerical simulations. The trimmer mesh algorithm was used to have a fully hexahedral mesh structure in the computational domain. A prism layer was used to model the boundary layer flow around the ship model. The all-wall y^+ approach was employed as the wall function, and the near-wall region was resolved keeping the wall y^+ around 1, especially on the flight deck surface. The maximum wall y^+ value was about 29. The maximum value was achieved on the ship's surfaces without any separation, rather than in critical regions such as the flight deck. Because the critical flight deck region was highly resolved down to $y^+ \approx 1$ without relying on wall functions, the IDDES all-y^+ wall treatment accurately captures the shear layer separation and preserves the integrity of the computed unsteady velocity fluctuations in the airwake. The total number of cells is about 28.86×10^6. The IDDES analyses for the ship airwake were performed at a scale of 1/50, based on the NATO-GD model scale in the open literature.[2]

In the present study, the effects of ABL and wind angle were investigated. Therefore, the entire ship was modeled rather than using a half-body approach. For the numerical setup, the inlet and the top surfaces were defined as velocity inlets, while the outlet surface was specified as a pressure outlet. The hull geometry and the bottom surface were defined as no-slip walls. During the numerical analyses, 4400 time steps were solved, and the last 4000 were used to compute time-averaged data. The study of Whitehouse *et al.*[21] used a time step between 0.02 and 0.04 s, while the study of Fernandez *et al.*[22] kept the time step as 0.01 to obtain the spectral results up to 25 Hz. Both studies used the IDDES/LES turbulence model instead of the unsteady RANS model for detailed characterization of turbulent flow. The time step size was chosen as 5×10^{-3} s. The numerical analyses were run for 22 s of physical time. The first 2 s were entirely discarded to bypass the initial numerical transient and ensure flow development. Only the fully developed, statistically stationary last 20 s were used for the spectral and wavelet analyses. The spectral and scalogram analyses were conducted in a wide frequency band up to 100 Hz. Similarly, 20 s of data were collected in the reference experimental study[2] of NATO-GD benchmark model with the same time step. In addition, in most of the studies given in the literature review, sampling frequency is 200 Hz while Nyquist frequency is 100 Hz, which is high enough for covering the turbulent structures and flow behaviors behind the superstructure.

For the model-scale simulations ($L_{WL} = 3$ m) at a reference velocity of 10.3 m/s, the characteristic flow-through time is approximately 0.29 s. The analyzed 20-s signal captures roughly 68 convective times, which is highly sufficient to ensure statistical stationarity for the turbulent flow structures.

C. Atmospheric boundary layer and dynamic similarity

Many studies on ship aerodynamics have ignored the effects of the ABL, while others have considered them. In this study, the effects of the ABL on the ship airwake were investigated using an ABL profile[23] similar to the power law profile.[24] The velocity profile defined at the inlet is a steady ABL, neglecting turbulent effects over time. The turbulent fluctuations in the ABL profile were neglected since the primary unsteady effects in the turbulent structures over the flight deck are driven by the superstructure itself

$$u^* = K\frac{uref}{\ln\left(\frac{z_{ref} + z_0}{z_0}\right)}, \tag{12}$$

$$u(z) = \frac{u^*}{K}\ln\left(\frac{z + z_0}{z_0}\right). \tag{13}$$

Here, z_{ref} is the reference height (0.60 m) where the wind anemometer is located, and u_{ref} is the reference velocity (10.3 m/s), considering the relative wind velocity is 20 knots. The reference velocity is kept the same as in the reference studies.[2,8] z_0 is the aerodynamic roughness length considered as 0.0002 to represent the free surface as described in the guidelines,[25,26] while u^* is the friction velocity. K is the von Karman constant and is considered to be 0.40. The effects of the ABL and uniform velocity profiles have been presented in a previous study by the authors, showing that the ABL profile yields a more realistic velocity field.[8,27] Previous studies[24,28,29] have shown that the flow field

18 November 2026 10:48:16

Published under an exclusive license by AIP Publishing

over the flight deck is independent of the Reynolds number. The dynamic similarity rule for the ship airwake is satisfied by the Strouhal number, and it is expressed as

$$\left(\frac{f_s}{f_m}\right)\cdot\left(\frac{L_s}{L_m}\right)\cdot\left(\frac{U_m}{U_s}\right)=1. \tag{14}$$

D. Frequency (spectral) and time-frequency (spectrogram) analysis methodology

In this study, the unsteady characteristics of the ship airwake, especially the velocity fluctuations, were analyzed using spectral and time-frequency decomposition methods. These methods were employed to characterize the dominant flow structures and the energy distribution of these turbulent structures. The methodology for each analysis method was briefly presented. The frequency-domain characteristics of the unsteady airwake were obtained in terms of velocity fluctuations using the fast Fourier transform (FFT) method.[30] For a given discrete time-domain signal $x[n]$ consisting of N samples, the transformed sequence $X[k]$ is defined as

$$X[k]=\sum_{n=0}^{N-1}x[n]e^{-i\frac{2\pi}{N}kn}, \tag{15}$$

where k is the frequency index from 0 to N, n is the discrete time index, and i is the imaginary unit. The FFT output provides an amplitude-phase representation over the analyzed time window to identify dominant flow structures, such as vortex-shedding frequencies originating from the ship's superstructure. To quantify the distribution of the turbulent kinetic energy across the frequency spectrum, the power spectral density (PSD) method[31,32] was employed. The PSD function, $S_{xx}(f)$, for a wide range of frequencies, can be estimated from the squared magnitude of its Fourier transform normalized by the observation time T

$$S_{xx}(f)=\lim_{T\to\infty}\frac{1}{T}\left|\int_{-T/2}^{T/2}x(t)e^{-i2\pi ft}dt\right|^2. \tag{16}$$

In the ship airwake analysis, the PSD output gives the energy distribution across different scales. The output is typically expressed in variance per unit frequency, $(m/s)^2/Hz$ in this study, since the input is the velocity component. In addition, the root mean square of the area under the PSD plot gives the turbulent fluctuation velocity (e.g., u', v', w') which can be used to calculate the turbulent intensity of each direction and the three-dimensional turbulent kinetic energy. The PSD curves are windowed using a Hanning function with a 50% overlap to reduce spectral leakage. The relation between PSD, velocity variance, TKE, and TI is given briefly below

$$\sigma_u^2=\overline{u'^2}=\int_0^{f_{\max}}S_{uu}(f)df, \tag{17}$$

$$u'_{RMS}=\sqrt{\overline{u'^2}}. \tag{18}$$

Equations (17) and (18) can be derived also for other velocity components. Then turbulence kinetic energy (TKE) and turbulence intensity (TI) can be obtained as follows:

$$TKE=\frac{1}{2}\left(\overline{u'^2}+\overline{v'^2}+\overline{w'^2}\right), \tag{19}$$

$$TI_u=\frac{u'_{RMS}}{U_{ref}},\quad TI_v=\frac{v'_{RMS}}{U_{ref}},\quad TI_w=\frac{w'_{RMS}}{U_{ref}}. \tag{20}$$

The spectral analysis described above cannot provide time-varying frequency information. To obtain frequency information over time, a localized time-frequency analysis is required. Time-frequency representation creates a 2D image by separating the signal into its time and frequency components. The transforms used in this study are used in fields such as machine fault detection, biomedical signal processing, and seismology. Because of the highly unsteady nature of ship airwakes, continuous wavelet transform (CWT) was employed for time-frequency analysis. The CWT method,[33–35] using the Morlet function as the mother wavelet function, optimizes time resolution at high frequencies and frequency resolution at low frequencies. The CWT of a signal $x(t)$ is computed by convoluting the signal with a scaled and translated mother wavelet function, $\psi(t)$

$$W_x(s,\tau)=\frac{1}{\sqrt{s}}\int_{-\infty}^{\infty}x(t)\psi^*\left(\frac{t-\tau}{s}\right)dt, \tag{21}$$

where $W_x(s,\tau)$ represents the wavelet coefficients, s is the scale parameter, τ is the translation parameter, ψ^* denotes the complex conjugate. This transform provides a localized time-frequency representation, revealing both dominant spectral components and their precise temporal occurrence. During this process, the CWT coefficients, $W_x(s\tau)$, represent the instantaneous amplitude of velocity fluctuations at a given frequency and time. The squared magnitude of these coefficients, $\left|W_x(s\tau)\right|^2$, gives the local wavelet power spectrum. By integrating this power spectrum over a specific frequency band, we obtain the instantaneous variance (energy) of the velocity fluctuation in that band. The square root of this variance yields the instantaneous RMS velocity fluctuation, which is then normalized by the reference velocity (10.3 m/s) to calculate the instantaneous TI. The relation between wavelet coefficients, velocity fluctuations, RMS velocity and instantaneous TI are given briefly below

$$\sigma^2(\tau)=\frac{1}{C_\delta}\int_{s_1}^{s_2}\frac{|W_x(s,\tau)|^2}{s}\cdot\chi_{COI}(s,\tau)\,ds, \tag{22}$$

$$u'_{RMS}(\tau)=\sqrt{\sigma^2(\tau)}, \tag{23}$$

$$TI(\tau)=\frac{u'_{RMS}(\tau)}{U_{ref}}. \tag{24}$$

For signal processing of the numerical results, the sampling frequency is 200 Hz with a frequency resolution of 0.05 Hz. Hence, the Nyquist frequency is calculated as 100 Hz. The 20-s interval captures approximately 20–40 cycles of the dominant low-frequency shedding structures (typically occurring around 1–2 Hz), which is sufficient to achieve statistical convergence for the primary energy-containing scales. For CWT, the Morlet wavelet parameter is considered as $\omega_0 = 6$ for scale-to-frequency conversion. The cone of influence (COI) was implemented in the CWT method, as presented in the equations, considering the folding time as $\sqrt{2}$ s. In addition, edge effects were mitigated by applying a zero-padding technique before the CWT computation

18 November 2026 10:48:16

Published under an exclusive license by AIP Publishing

$$\chi_{COI}(s,\tau) = \begin{cases} 1, & s \le \dfrac{\Delta t_{edge}(\tau)}{\sqrt{2}}, \\ 0, & s > \dfrac{\Delta t_{edge}(\tau)}{\sqrt{2}}. \end{cases} \tag{25}$$

III. RESULTS AND DISCUSSION

The numerical results are presented for various WOD angles ranging from R30° to G30°. Unsteady IDDES analyses were performed to obtain time-series data for three velocity components. The coordinate system is at the intersection of the hangar wall and the flight deck. The numerical results were validated at these points as dictated in the reference experimental study.[2] Using the validated numerical setup with a DES grid and turbulence model, new DES simulations were conducted for headwind and all asymmetric WOD angles. The newly obtained time-series velocity data were used for frequency analysis with an FFT, and PSD analyses were carried out to calculate the spectral variance in the frequency domain. The variance of the velocity, turbulence intensity, and turbulent kinetic energy at each point was calculated. Finally, time-frequency analyses were made using CWT to obtain the wavelet scalogram at each measurement point.

Figure 1 shows the flow chart of data processing steps in this study. The raw time-series data were obtained for three velocity components. The equations for the turbulence kinetic energy and turbulence intensity using PSD curves were given in the previous chapter. Also, the equations for the instantaneous TI using CWT scalograms were given. Using the fluctuating velocity components (e.g., u', v', w'), the three-dimensional turbulence intensity was calculated and expressed as

$$TI_{3D} = \frac{\sqrt{\frac{1}{3}\left(\overline{u'^2} + \overline{v'^2} + \overline{w'^2}\right)}}{U_{ref}}. \tag{26}$$

For a fair comparison, three-dimensional TI was calculated as given in Eq. (26), as recommended in Ref. 36. TKE was also non-dimensionalized and expressed as

$$TKE_{\%} = 100 \cdot \frac{TKE}{{U_{ref}}^2}. \tag{27}$$

Both the turbulence kinetic energy and turbulence intensity were non-dimensionalized using the reference velocity (10.3 m/s) instead of local mean velocity since the local mean velocity may approach zero in the wake regions and this leads to asymptotic, physically misleading TI values. Therefore, in aerodynamic studies, it is standard practice to normalize the fluctuations by the free-stream reference velocity.[10] The WOD angles of 15° and 30° were specifically selected to represent the critical crosswind limits of typical SHOL envelopes.

A. Numerical validation of ship airwake

The validation of the numerical results was performed for three different velocity components, as given in the authors' recent study[8] on headwind conditions, by comparing with the available experimental results.[2] Figure 2 shows a comparison of the results in terms of longitudinal velocity, as an example. The validation of lateral and vertical velocity components was also made. The details of the validation in all components and the numerical uncertainty can be found in the authors' reference study.[8] Validation of the numerical setup was made in terms of velocity components since there is no experimental time-series or spectral data. The present study aims to present a numerical baseline for ship aerodynamics topology, showing the spatial and temporal trends of turbulent structures over the flight deck. The verification study was also carried out in the reference study; detailed information can be found similar to the validation results. Grid uncertainty was calculated with different methods based on the grid convergence index (GCI), and the numerical uncertainty was found to be <2%. As stated in the reference study,[8] the verification study was conducted for unsteady RANS analyses, and the mesh algorithm was revised to achieve denser mesh resolution (IDDES) around the flight deck region. A validation study was conducted on both URANS and IDDES mesh structures. As shown in Fig. 2, the comparison exhibits good correspondence, demonstrating that the IDDES-based numerical model

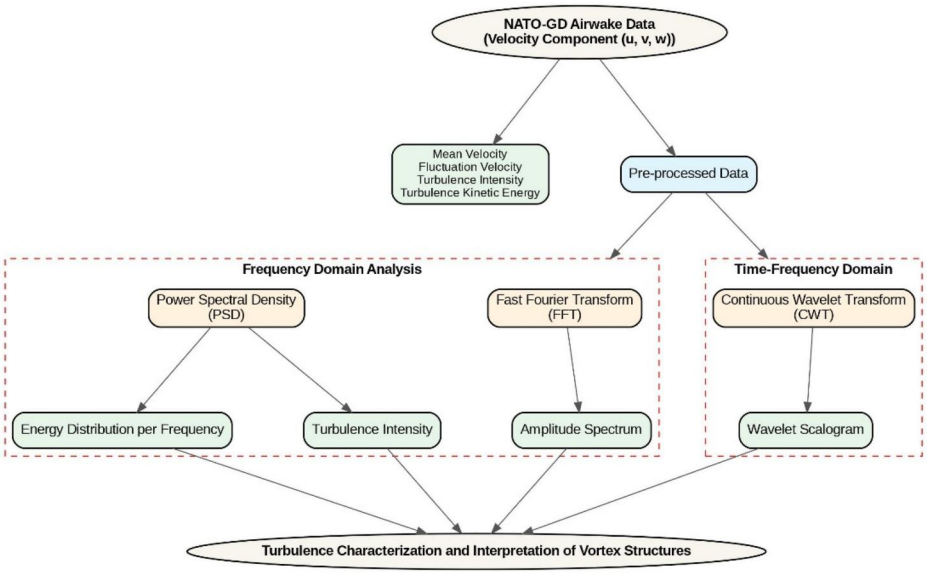


FIG. 1. Flowchart for data processing of raw time-series data obtained by DES analyses.

18 November 2026 10:48:16

Published under an exclusive license by AIP Publishing

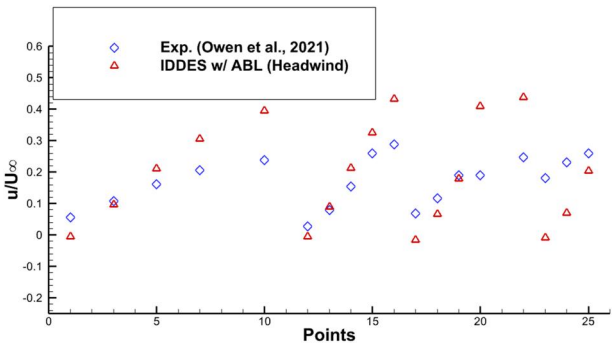


FIG. 2. Numerical and experimental results for validation.

accurately captures the essential flow physics of the ship airwake in terms of the u-component of the velocity. After the validation study given in Ref. 8, numerical simulations were extended for WOD angles between R30 and G30. In short, all analyses in this study are new and based on the numerical framework of the authors' reference study.[8] Spectral results are presented for the first time in this study.

B. Turbulence characterization

The spectral analysis methods shown in the flow chart were applied to the raw time-series data for different velocity components at the WOD angles. The turbulence kinetic energy and turbulence intensity values were calculated at each point, and the scalar contours were obtained. The following figures present details of the turbulent flow by showing turbulence kinetic energy and turbulence intensity. In addition, three different velocity components were also presented in the figures, including the streamlines in the YZ plane section. Scalar contours of velocity distribution, TI, and TKE for XZ and XY planes are given as Supplementary Material. To generate continuous scalar contours from these discrete data points, a piecewise cubic, continuously differentiable interpolation algorithm was employed using Python.

In the experimental reference of the NATO-GD model,[2] there are only 18 points located in the mid-section of the flight deck, and these points do not cover the region from port to starboard side, and this situation hinders the interpretation of the flow on the starboard and port sides at different wind angles. Therefore, 75 points covering the entire region along the starboard-port axis, positioned from the hangar wall toward the stern in the profile view, were used.

XZ-plane sections show that the flow separations become visible on the port and starboard sides in different wind scenarios. XZ-plane sections provide insight into the crosswind gradients over the flight deck. The lateral velocity and the streamlines show similarities for the outermost points on the port and starboard sides. The outermost port section in R30 condition resembles the outermost starboard section in G30 condition. However, the velocity field and streamlines show differences between the inner port and starboard sections under R15 and G15 conditions. The wind scenarios of 15° and 30° produce large cross-vortex structures. At the same time, in the centerline section, the streamlines show reattachment to the flight deck, and the flow separations remain in the outermost sections on both the port and starboard sides.

According to the vertical velocity component and the streamlines in XY sections, vertical velocity fluctuations are a primary limiting factor in helicopter operations, as fluctuations exceeding 1.75 m/s directly dictate operational limits.[37,38] Headwind conditions indicate that the bottom and lower-mid sections have a noticeable vortex structure, while the flow exhibits symmetrical recirculation. From the middle of the deck, the flow tends to gather. In port and starboard conditions of 15° and 30°, the symmetrical recirculation zone is completely disrupted, pushing toward the leeward side of the deck. Flow separation from the deck edges creates high-velocity jumps, especially at the windward edges. At lower elevations, the spiral nodes in the streamlines perfectly mark the vortex cores.

Figure 3 shows the longitudinal velocity component and the streamlines in YZ sections. Longitudinal velocity is the one that may subject the helicopter rotor to asymmetric loading due to longitudinal vortices. At wind angles of 15° and 30°, longitudinal vortices with localized turbulence intensities exceeding 20% formed, apparently originating from the windward hangar corner and extending along the flight deck. These structures exhibit a topology like leading-edge vortices. The low-speed zone behind the hangar gradually recovers as it moves backward along the flight deck, but in crosswinds, this recovery is asymmetric, with the plane drifting downwind. In headwind conditions, symmetrical downwash streamlines descending from top to bottom in the transverse planes clearly confirm that the flow descends over the hangar onto the deck.

The velocity distribution, presented in matrix form at different cross sections across the flight deck, reveals the velocity field behind the hangar. It should be emphasized that the identification of coherent structures and periodic vortex shedding is not based solely on velocity-spectrum signatures. The spatial organization of these structures is supported by the streamlines (v, w) and perpendicular mean velocity contours presented in Fig. 3. The spatial evidence demonstrates the physical roll-up of the shear layer originating from the hangar corners, providing the necessary flow-field evidence that confirms the structural topology responsible for the dominant frequencies observed in the subsequent spectral analysis.

The turbulence intensity was calculated using Eqs. (20) and (26); the turbulence fluctuation velocities were calculated using the PSD method on the raw time-series data. The variance of the PSD, which is the area under the PSD curve, is the square of the fluctuation velocity. Each fluctuation velocity was calculated, and the three-dimensional turbulence intensity was then obtained. The contours in matrix form for different wind-over-deck angles were presented in percentage. According to the three-dimensional turbulence intensity in XZ sections, the contours show that a high-turbulence recirculation zone ($TI > 15\%$) becomes visible, starting behind the hangar and extending to the middle of the deck. At stagnation points within the recirculation regions, the turbulence intensity reaches its maximum. In crosswind scenarios, the difference in TI becomes very sharp for the windward and leeward sections. While the windward sections are under the laminar flow effect, the leeward sections show a highly detached flow regime because of the turbulent fluctuations caused by the sharp edges of the hangar bay.

According to the three-dimensional turbulence intensity in XY sections at different elevations, in headwind conditions, the turbulent flow becomes symmetrical by the time it reaches the flight deck. In crosswind conditions, turbulence intensity reaches its maximum

18 November 2026 10:48:16

Published under an exclusive license by AIP Publishing

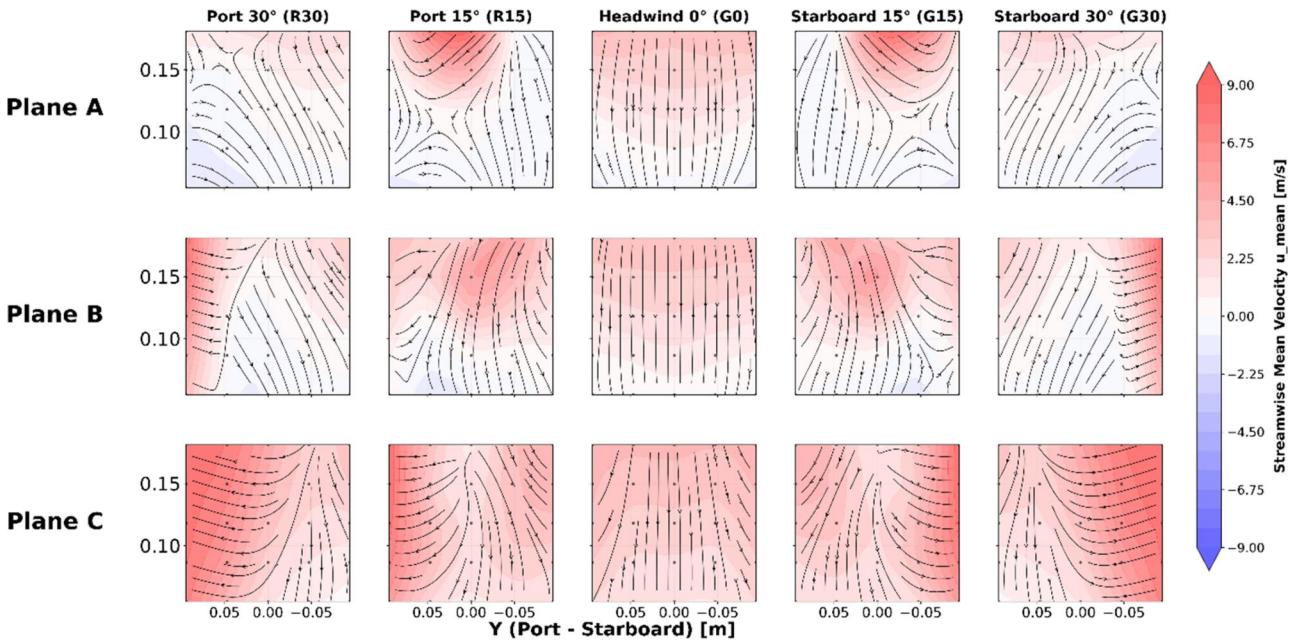


FIG. 3. Perpendicular mean velocity (u_{mean}) and streamlines (v, w) in YZ planes.

behind the hangar bay in the top and upper sections, while it decreases across the entire width in the lower sections near the flight deck. The maximum value of the turbulence intensity moves from the leeward to the windward direction while descending from the top section toward the flight deck.

Figure 4 shows the three-dimensional turbulence intensity in YZ sections. In crosswind scenarios, the centers of longitudinal vortices, characterized by localized TI values exceeding the 15% threshold, traverse from the hangar bay toward the ship stern. Especially at 30° wind angles, the turbulence intensity exceeds 20%. These are the bubble regions where the velocity is very low, but the velocity fluctuations are significant. From the hangar bay toward the ship's stern, the turbulent, high-intensity flow descends and spreads toward the flight deck.

Furthermore, TI values can be evaluated based on specific percentages, providing clearer insights into safe helicopter operations.[10] In accordance with existing civil aviation regulations,[37,38] a simplified assumption was made to establish safe limits for turbulence intensity and turbulence kinetic energy. According to these regulations, the vertical fluctuation velocity must not exceed 1.75 m/s, whereas the maximum allowable longitudinal fluctuation velocity is 5 m/s. To calculate the three-dimensional turbulence intensity, a maximum limit of 1.75 m/s (Refs. 37 and 38) was assumed for each fluctuation velocity component, with a reference wind speed of 10.3 m/s. Consequently, the TI limit was calculated to be approximately 17%; however, a more conservative limit of 15% was adopted for this study. The regions behind the hangar bay that exceed these limit values will be further examined using time-frequency analysis in the subsequent chapter. Flow diverging from the hangar causes a velocity deficit in the wake region behind the hangar, while increasing velocity fluctuations to TI levels above 15%. Three-dimensional TI is the most critical parameter in the ship's airwave topology, as it represents the ratio of these fluctuations to the average speed. At 0°, flow divergence is symmetrical and limited, while a 15° deviation triggers the merging of flows from the side and roof, creating large-scale vortex structures (characteristic frequencies of 0.1–5 Hz) and covering the entire deck with a turbulent layer where TI exceeds the 15% threshold. At larger angles (30°), this vortex structure spreads over a wider area and drifts to one side.

In the case of headwinds, the visual evidence perfectly demonstrates that the flow does not violate the 15% TI limit in any area, with the volume remaining empty. In crosswinds (15° and 30°), the clean areas (low TI) in the leeward region are filtered out, leaving the significant violation volume created by the windward shear layer and the central recirculation bubble.

The turbulence kinetic energy was calculated using Eqs. (19) and (27). To ensure a fair comparison, the three-dimensional turbulence kinetic energy (TKE) was non-dimensionalized using the square of the reference wind velocity, and the results were presented as a percentage. Furthermore, although the non-dimensional TKE limit was calculated to be approximately 4.3%, a 5% threshold was adopted for this study. According to three-dimensional turbulence kinetic energy in XZ sections, from all angles, the turbulent shear layer formed as the flow separates from the hangar roof exhibits non-dimensional TKE values concentrated between 5% and 8.75%. In crosswinds, the flow sweeps the deck with a high TKE in the lateral sections on the windward side (e.g., "Port Outer" for Port 30°). In contrast, TKE values remain relatively low on the leeward side (e.g., "Starboard Outer" for Port 30°). However, these low TKE regions are the areas where complex recirculations occur. Therefore, although the average TKE is low, the swirling flow character dominates.

According to the three-dimensional turbulence kinetic energy in XY sections, these horizontal sections show the horizontal trace of the separated flow and the distribution of turbulence that may affect the helicopter's rotor disk plane. In both Port 15° and Starboard 15°

18 November 2026 10:48:16

Published under an exclusive license by AIP Publishing

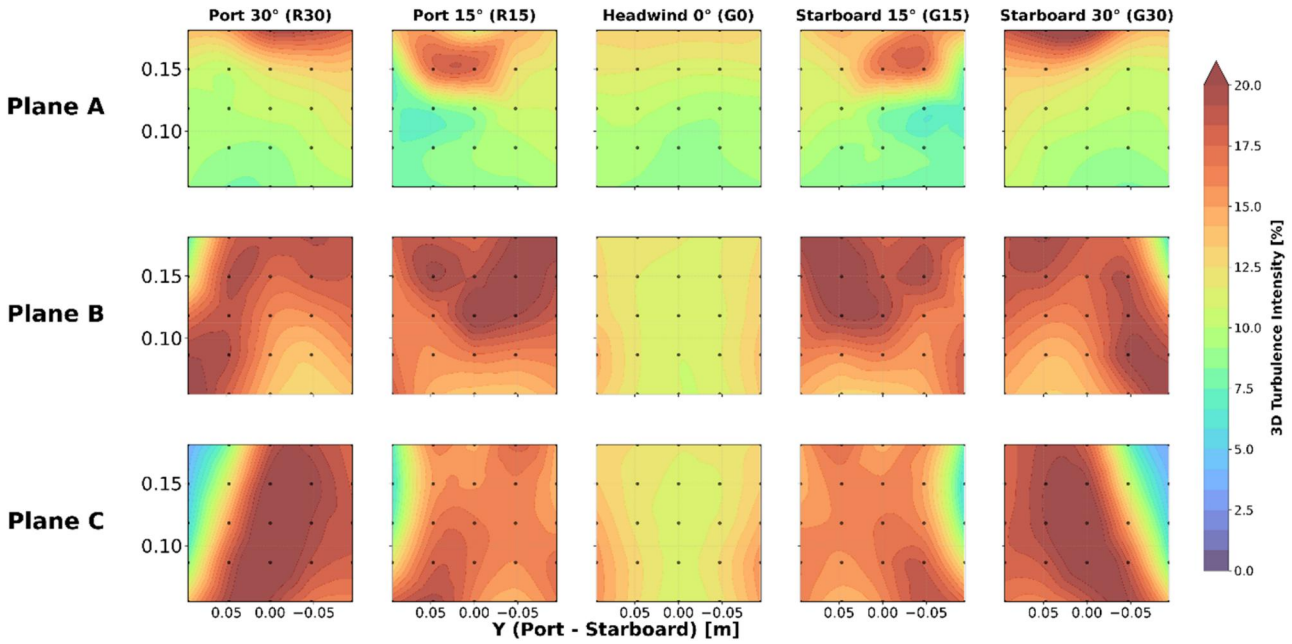


FIG. 4. 3D Turbulence intensity distribution in YZ planes.

cases, there are highly concentrated TKE peaks at the mid and upper deck levels ($Z = 0.118$ m and $Z = 0.150$ m). These localized high-energy regions are where the shear layer rolls and turbulent fluctuations reach their maximum. In terms of the Helicopter-Ship Dynamics Interface, these red/orange points indicate localized high-energy regions that pose potential aerodynamic hazards. Because this study evaluates an isolated ship airwake without a coupled rotor-load calculation, future flight-dynamics simulations are required to precisely quantify the resulting pilot workload. At 30° angles, the turbulent region spreads over a wider area, but instead of creating a TKE peak as narrow and sharp as in the 15° case, it distributes the energy over a wider band toward the leeward region.

Figure 5 shows the three-dimensional turbulence kinetic energy in YZ sections. For the headwind condition, the TKE distribution is quite low and symmetrical. The energy density is more homogeneously dissipated in the areas closer to the deck and in the center of the hangar wake. At 15° and 30° angles, the flow breaking off from the windward hangar corner generates localized high TKE regions peaking above 8.75%. The longitudinal vortex cores in the velocity contours appear here as regions of maximum turbulence production. As moving from Plane A ($X = 0.118$ m) to Plane C ($X = 0.354$ m), the high-energy turbulent structure descends to lower Z-elevations and spreads across a wider lateral area. Mechanistically, this spatial expansion indicates that the concentrated shear layer dissipates into broader, intermittent turbulent fluctuations along the approach path, directly driving the increased high-turbulence fractional times observed in the subsequent time-frequency analysis.

At 0° wind angle, none of the nodes on the measurement grid exceed the 5% TKE limit (all nodes are light blue). The energy contained within the symmetrical recirculation zone formed behind the hangar does not reach a level that would restrict helicopter operations. This confirms that the headwind offers ideal aerodynamic conditions for approach and landing. At 15° of deviation, the red dots cluster in a very specific, narrow volume. These clusters indicate the core of the main longitudinal vortex formed by the rolling of a shearing layer that broke off from the windward hangar corner. The zones exhibiting TKE > 5% are predominantly located in the middle deck distances (around Plane B, $X = 0.236$ m) and at mid- to upper altitudes ($Z > 0.10$ m), leaning toward the windward side. This creates an essentially high-energy, invisible "turbulence wall" that the helicopter must overcome on its approach path. When the wind angle increases to 30°, the concentrated turbulence at 15° is replaced by a wide corridor of turbulence that crosses the deck diagonally. The red dots are on the windward side and at high altitude near the hangar (Plane A); as the windward wind progresses toward the leeward side and at lower altitudes (downward on the Z-axis), it is swept toward the leeward side and to lower altitudes. The increasing crosswind component pushes the wake region outward from the deck, and this expanding diagonal volume exposes the helicopter to the high TKE region for an extended period during approach.

C. Time-frequency analysis

Numerical simulations were performed at a wind speed of 10.3 m/s with an ABL-based velocity profile. Five relative wind angles were investigated to comprehensively evaluate aerodynamic interactions under varying conditions: Port 30° (R30), port 15° (R15), headwind (0°), starboard 15° (G15), and starboard 30° (G30). For each wind condition, velocity time series were obtained from a grid of measurement points located in a specific order to capture the complex flow field characteristics and turbulent structures within the ship's airwake. As shown in Fig. 6, the data points were distributed across three

18 November 2026 10:48:16

Published under an exclusive license by AIP Publishing

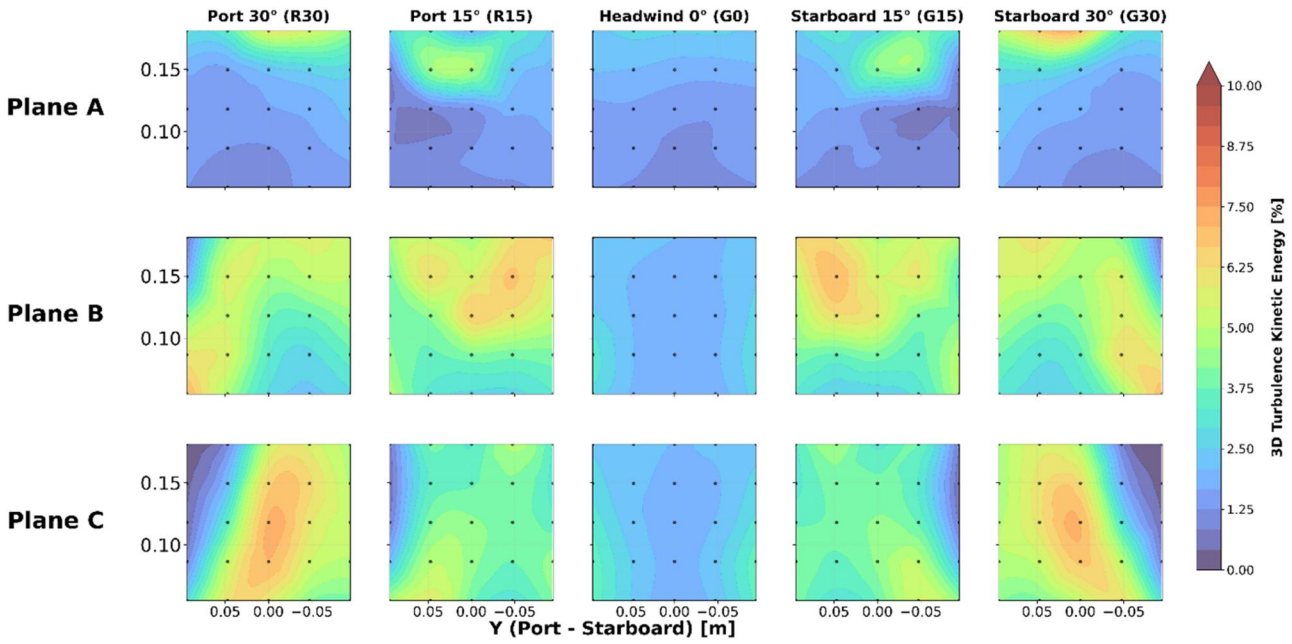


FIG. 5. Turbulence kinetic energy distribution in YZ planes.

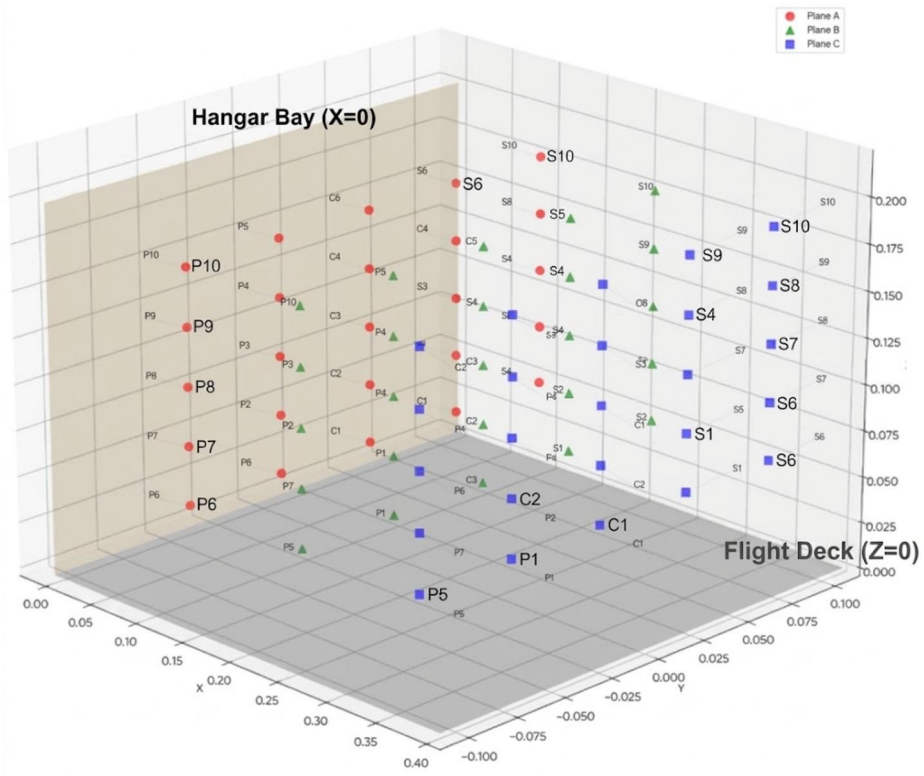


FIG. 6. 3D visualization of the measurement point locations.

18 November 2026 10:48:16

Published under an exclusive license by AIP Publishing

transverse planes (Planes A, B, and C), with the hangar surface defined as the origin (X = 0) for the longitudinal axis and the flight deck as the vertical reference (Z = 0). The transverse planes were positioned at X = 0.118 m, X = 0.236 m, and X = 0.354 m, respectively. Each plane consists of 25 precisely positioned points spread along the transverse and vertical axes. The notation "C" is for the centerline, while "P" stands for the port side and "S" stands for the starboard side. The flow data collected at these coordinates were used in spectral analyses, and the turbulence characterization was detailed in Sec. III B. Within this detailed turbulent flow investigation, Continuous wavelet transform (CWT) analyses were conducted at all measurement points to investigate the transient nature of the airwake under different wind conditions.

To the best of the authors' knowledge, few studies have focused on CWT analysis of time-domain velocity data for ship airwake.[9,39–41] These studies mostly rely on the ship-helicopter interaction using the SFS2 model, and no scalograms were presented directly to show the time-frequency response of the vortex structures. The relationship between wavelets and turbulent flow was emphasized in early studies.[33,34] The CWT method enables observation of coherent structures in both the time and frequency domains. The CWT analysis was applied to the pilot's collective control inputs and to aerodynamic force and moment fluctuations on the rotor. On the other hand, the present study focuses on CWT analysis to determine the time-frequency response of the time-series velocity data at different WOD angles. The CWT scalograms were obtained for all measurement points at different WOD angles for longitudinal, lateral, and vertical velocity components. Using these CWT scalograms, two-dimensional turbulence intensity distributions were obtained instantaneously. The time-frequency scalograms are used in conjunction with the spatial streamline and velocity vector fields (Fig. 3). The temporal energy shifts observed at specific points are interpreted as local spectral signatures corresponding to the passage and breakdown of structures whose spatial presence is verified by the flow field topologies.

Time-frequency analysis was performed across the entire flow volume using scalograms obtained from all 75 points. Thus, the turbulence intensity (TI) over the flight deck could be examined in detail not only with one-dimensional and time-averaged values obtained with conventional FFT and PSD methods, but also with a two-dimensional and instantaneous (time-dependent) dimension. The fractional-time calculation was made using Eq. (28) as given below

$$F_t = \frac{1}{T_{\text{total}}} \int_0^{T_{\text{total}}} \mathcal{H}(\text{TI}(t) - \text{TI}_{\text{threshold}})dt, \tag{28}$$

$$\mathcal{H}(x) = \begin{cases} 1, & x > 0, \\ 0, & x \leq 0. \end{cases} \tag{29}$$

Here, $\mathcal{H}(x)$ is the Heaviside function for defining the condition. T_{total} is the total time after considering the cone of influence (COI), and the threshold for TI is 15%.

Figure 7 shows the high occurrence of turbulence across different velocity components at different WOD angles. The occurrence was determined by identifying the time sequences of instantaneous turbulence intensity exceeding 15% across different frequency bands in the CWT scalograms. As shown in the example above, instances when turbulence intensity (TI) exceeded 15% were detected across different frequency bands using CWT scalograms from all measurement points, and fractional time analysis was applied to the resulting data. This approach calculated the percentage of total time during which the TI exceeded the 15% threshold as a function of wind over deck (WOD) angles, thereby characterizing whether the computed aerodynamic disturbance was temporary or continuous, which serves as a physical basis for inferring potential flow-related operational risks.

While spectral techniques identify the dominant frequencies, relying on a velocity-spectrum signature is insufficient to establish the spatial organization of complex shedding phenomena such as Kármán-type vortex streets. Therefore, the localized time-frequency energy shifts observed in the CWT scalograms are directly coupled with the spatial flow-field evidence previously established in the YZ planes. The correlation between the structural expansion of the longitudinal vortices (Figs. 3 and 4) and the corresponding frequency-band fractional times confirms that the observed spectral peaks are direct manifestations of the physical vortex shedding and its spatial evolution along the flight deck.

The spectral evaluation was divided into three distinct bands based on the physical rotor characteristics of a standard naval helicopter (e.g., S-70 operating at 258 RPM). The low-frequency band (0.1–5 Hz) encompasses the main rotor frequency (4.2 Hz) and large-scale vortex shedding, which are critical for global stability. The mid-frequency band (5–20 Hz) covers the blade pass frequency (16.8 Hz), where turbulent energy can induce asymmetric rotor loading and cyclic forcing. Finally, frequencies above 20 Hz represent a high-frequency dissipation range, which lacks the kinetic energy to significantly alter flight dynamics and is, therefore, evaluated separately.

For the 0.1–5 Hz band, it is observed that exceedance rates range from 87% to 96% across all velocity components (u, v, w) and all wind angles. This indicates that low-frequency, large-scale flow fluctuations constitute the most dominant characteristic at all angles.

For the 5–20 Hz band, the exceedance rates generally range between 66% and 80% (e.g., reaching 79.6% at G15 for the lateral component), confirming that medium-scale turbulence energy exceeds the 15% threshold for a significant proportion of the time. This sustained medium-frequency energy dynamically corresponds to the lateral spreading of the longitudinal vortices observed in the YZ planes (Fig. 7); as the physical vortices expand toward the stern, they manifest temporally as a continuous medium-frequency aerodynamic disturbance. At medium frequencies, the peak percentage value decreases to 66% for the vertical velocity component, while other components show a similar occurrence ratio.

For high frequencies over 20 Hz, the durations for which high-frequency, small-scale fluctuations exceed the $TI > 15\%$ threshold are quite low. While these rates remain around 1%, particularly at the headwind condition, they rise to levels of 12%–16% in angled scenarios (especially regarding the v and u components).

Before conclusions, it should be noted that the simulations in the present study were carried out at a single reference wind speed (10.3 m/s) across a set of asymmetric WOD angles. Furthermore, the numerical framework used a steady Atmospheric Boundary Layer (ABL) inlet profile and evaluated an isolated, captive ship model. This study establishes a baseline aerodynamic topology, including the signal processing processes for detailed flow field investigations. Consequently, the ship in this study was kept as captive, so the free surface effects and ship motions were neglected to mimic the experimental wind tunnel conditions. Future studies may take these effects

18 November 2026 10:48:16

Published under an exclusive license by AIP Publishing

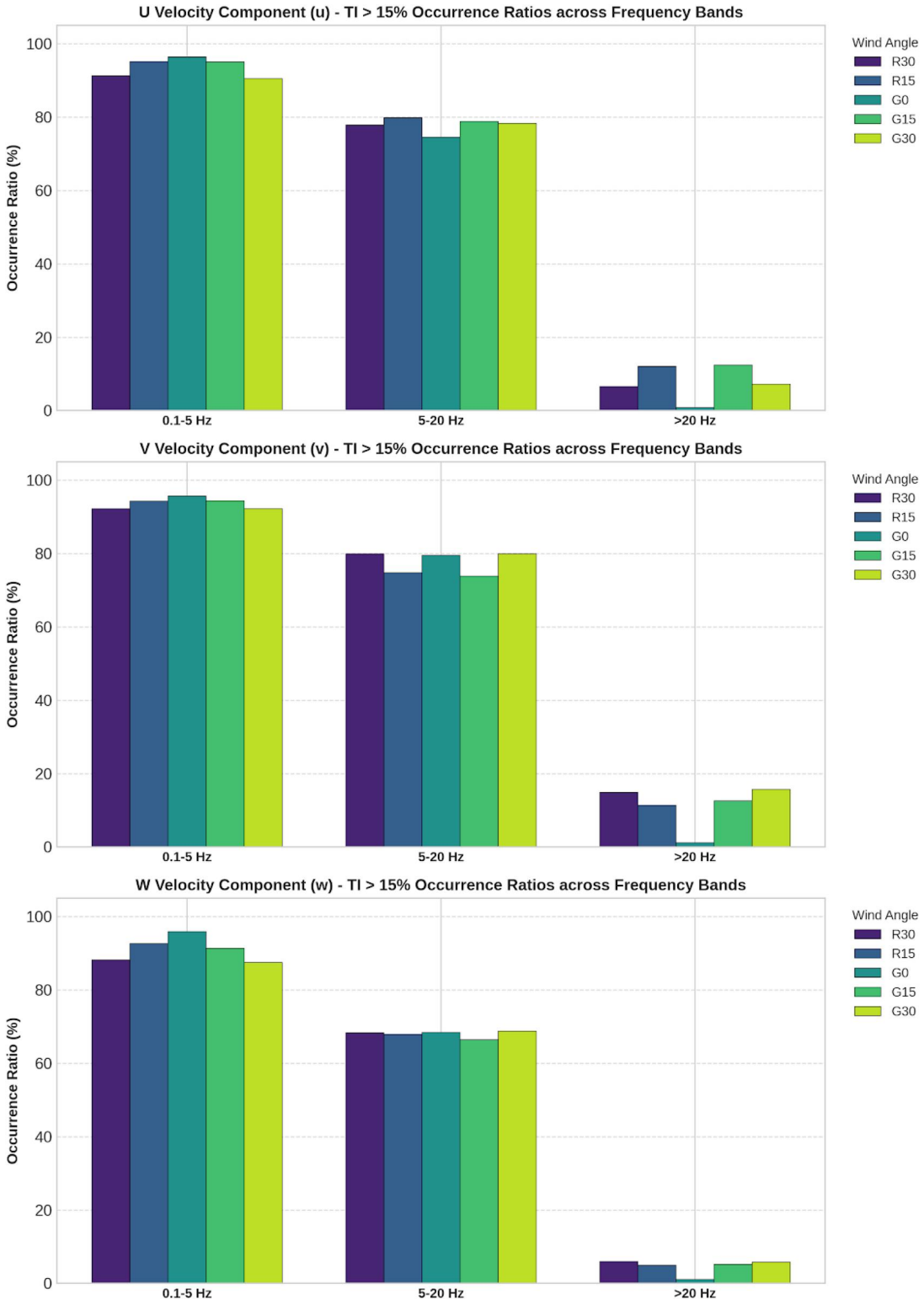


FIG. 7. High turbulence intensity occurrence.

18 November 2026 10:48:16

Published under an exclusive license by AIP Publishing

into account, and ship-rotor interactions can be evaluated with further studies.

IV. CONCLUSIONS

In this study, the highly unsteady and complex airwake of the NATO-GD model was investigated numerically with a non-uniform velocity profile based on ABL. High-fidelity IDDES simulations were performed for five different WOD angles (Headwind 0°, Port 15°/30°, and Starboard 15°/30°) at one wind velocity (10.3 m/s). A systematic signal-processing methodology was employed, combining fast Fourier transform (FFT), power spectral density (PSD), and continuous wavelet transform (CWT) analyses to comprehensively characterize the temporal and spatial nature of the coherent structures over the flight deck.

The spatial distribution of the 3D turbulence intensity (TI) and non-dimensional turbulent kinetic energy (TKE) revealed the sensitivity of the airwake topology to the WOD angle. In the headwind condition, the flow remains symmetrical, and the complex turbulent flow regime does not exceed the critical threshold of 15% TI. However, at asymmetric angles, high-energy turbulent flow detaches from the ship hangar corner, creating a high-energy turbulent region that reaches its maximum at 30° wind angles.

The localized time-frequency representation (CWT scalograms) and the fractional time analysis quantified the intermittency of these aerodynamic disturbances. A major finding of this study is the distinct behavior of the fluctuation velocity components across different frequency bands. For vertical velocity (w), the duration of high turbulence intensity ($TI > 15\%$) in the mid-frequency band (5–20 Hz) showed a stable trend between 67% and 69%, independent of the wind direction. This stability demonstrates that vertical vortex shedding is primarily governed by the hangar's backward-facing step geometry rather than by the angle of the incoming wind. Because the Strouhal number in the 5–20 Hz frequency band ranges between 0.08 and 0.32 using the hangar height, and the study of Owen *et al.*[2] also states that the large vortex breakdowns and shedding were observed at similar Strouhal numbers (0.10–0.30). On the other hand, for lateral (v) and longitudinal (u) velocities, while headwind conditions suppress high-frequency energy, crosswinds (especially at 30° angles) result in a significant shift of spectral energy toward higher frequency bands. The interaction of the flow with the sharp, asymmetrical corners of the superstructure shifts turbulent energy toward the high-frequency band (>20 Hz), reaching its absolute peak along the lateral axis. By coupling the spatial TKE distributions with the CWT fractional times, it is evident that the physical expansion of these longitudinal vortices from the hangar (Plane A) to the stern (Plane C) is the primary flow mechanism driving this spectral energy shift, thereby linking the spatial evolution of the airwake directly to frequency-dependent operational risks.

The aerodynamic results within the spectral and wavelet analyses reveal that low-frequency turbulent structures correspond to macro-scale vortices. This means that a helicopter approaching the ship superstructure remains entirely within this slowly oscillating air mass. The computed low-frequency vertical oscillations characterize the physical airwake topology. Because our analysis is an uncoupled aerodynamic assessment, these oscillations represent potential hazards that could alter lift forces and increase pilot workload; however, dedicated flight-dynamics simulations are necessary to quantify these operational consequences. Furthermore, the computed turbulent energy concentrated in the mid-frequency band (5–20 Hz) defines the aerodynamic environment, which is inferred as a potential risk factor for resonance with main rotor blades. The computed high turbulence intensity in the high-frequency band (>20 Hz) represents an aerodynamic feature that can be inferred as a potential operational risk for the tail rotor, which operates at much higher rotational speeds than the main rotor. Finally, rather than directly dictating safe helicopter operating limits (SHOL), these axis-specific and frequency-dependent aerodynamic disturbances highlight localized hazards. Time-frequency characterization of the isolated airwake serves as a foundational step, but coupled ship-helicopter simulations are required to precisely establish and quantify actual SHOL.

SUPPLEMENTARY MATERIAL

See the supplementary material for additional figures representing the NATO-GD model particulars, mesh structure, and boundary conditions. Some figures show examples of signal processing tools employed in the study. Figures about the measurement points and planes, and points having high turbulence properties, are also given.

The authors acknowledge the use of Google Gemini to assist with generating scripts for data processing, formatting figures, and language editing. All AI-generated output was carefully reviewed, verified, and edited by the authors, who assume full responsibility and accountability for the accuracy and originality of the final content.

ACKNOWLEDGMENTS

The authors also thank Navy Captain Mumin Murat Bozkurt of the Naval Aviation Command, Turkish Navy, for his insightful comments and support throughout this study.

AUTHOR DECLARATIONS

Conflict of Interest

The authors have no conflicts to disclose.

Author Contributions

Ali Dogrul: Conceptualization (lead); Data curation (equal); Formal analysis (equal); Investigation (equal); Methodology (equal); Software (equal); Validation (equal); Visualization (equal); Writing – original draft (equal); Writing – review & editing (equal). **Sarih Sari:** Formal analysis (equal); Investigation (equal); Methodology (equal); Software (equal); Validation (equal); Visualization (equal); Writing – original draft (equal); Writing – review & editing (equal). **Muhammet Taha Akkoc:** Formal analysis (equal); Methodology (equal); Visualization (equal); Writing – original draft (equal); Writing – review & editing (equal). **Seyfettin Bayraktar:** Project administration (lead); Writing – original draft (equal); Writing – review & editing (equal).

DATA AVAILABILITY

The data that support the findings of this study are available from the corresponding author upon reasonable request.

REFERENCES

[1]D. Seth, J. G. Leishman, E. Gnanamanickam, and Z. Zhang, "Time-resolved ship airwake measurements in a simulated atmospheric boundary layer," J. Aircr. **58**(3), 624–649 (2021).

18 November 2026 10:48:16

Published under an exclusive license by AIP Publishing

[2]I. Owen, R. Lee, A. Wall, and N. Fernandez, "The NATO generic destroyer—A shared geometry for collaborative research into modelling and simulation of shipboard helicopter launch and recovery," Ocean Eng. **228**, 108428 (2021).
[3]N. Fernandez, I. Owen, and M. D. White, "Baseline simulated ship-helicopter operating limits for the NATO generic destroyer," J. Aircr. **63**, 138 (2026).
[4]W.-H. Chen and J. Rauleder, "Wind tunnel investigation of a rotor under the influence of unsteady ship airwakes with azimuth-correlated measurements," in *Proceedings of the Vertical Flight Society 81st Annual Forum and Technology Display* (The Vertical Flight Society, Virginia Beach, VA, 2025), pp. 1–19.
[5]S. Polsky, "A computational study of unsteady ship airwake," AIAA Paper No. 2022-1022, 2002.
[6]P. Scott, I. Owen, and M. White, "The effect of ship size on the flying qualities of maritime helicopters," in *Vertical Flight Society 70th Annual Forum & Technology Display* (The Vertical Flight Society, Montréal, QC, 2014).
[7]D. Linton and B. Thornber, "Actuator surface modeling of rotors at the ship–helicopter dynamic interface," J. Aircr. **61**(5), 1461–1474 (2024).
[8]S. Sari, A. Dogrul, and S. Bayraktar, "Airwake characteristics of NATO-generic destroyer: A numerical study," J. Appl. Fluid Mech. **18**(1), 112–130 (2025).
[9]E. Kurban, B. Oates, M. J. Smith, and J. Rauleder, "Correlation of high- and mid-fidelity ship airwake analysis to experiment," J. Aircr. **62**, 857 (2025).
[10]J. S. Forrest, I. Owen, G. D. Padfield, and S. J. Hodge, "Ship-helicopter operating limits prediction using piloted flight simulation and time-accurate airwakes," J. Aircr. **49**(4), 1020–1031 (2012).
[11]W. Yuan, A. Wall, and R. Lee, "Combined numerical and experimental simulations of unsteady ship airwakes," Comput. Fluids **172**, 29–53 (2018).
[12]W. Yuan, A. Wall, E. Thornhill, C. Sideroff, M. Mamou, and R. Lee, "CFD-aided ship design and helicopter operation," J. Mar. Sci. Eng. **10**(9), 1304 (2022).
[13]A. Wall, E. Thornhill, H. Barber, S. McTavish, and R. Lee, "Experimental investigations into the effect of at-sea conditions on ship airwake characteristics," J. Wind Eng. Ind. Aerodyn. **223**, 104933 (2022).
[14]E. Kurban, S. Toxopeus, and J. Rauleder, "Assessment of Lattice-Boltzmann velocity set and floating-point precision for ship airwake analysis compared to RANS–LES and experiment," Ocean Eng. **326**, 120788 (2025).
[15]D. C. Wilcox, *Turbulence Modeling for CFD*, 3rd ed. (DCW Industries, La Cãnada, CA, 2006).
[16]D. C. Wilcox, "Formulation of the k-w turbulence model revisited," AIAA J. **46**(11), 2823–2838 (2008).
[17]M. S. Gritskevich, A. V. Garbaruk, J. Schütze, and F. R. Menter, "Development of DDES and IDDES formulations for the k-ω shear stress transport model," Flow, Turbul. Combust. **88**(3), 431–449 (2012).
[18]S. Shukla, S. N. Singh, S. S. Sinha, and R. Vijayakumar, "Comparative assessment of URANS, SAS and DES turbulence modeling in the predictions of massively separated ship airwake characteristics," Ocean Eng. **229**, 108954 (2021).
[19]E. Thornhill, A. Wall, S. McTavish, and R. Lee, "Ship anemometer bias management," Ocean Eng. **216**, 107843 (2020).
[20]N. A. Watson, M. F. Kelly, I. Owen, S. J. Hodge, and M. D. White, "Computational and experimental modelling study of the unsteady airflow over the aircraft carrier HMS Queen Elizabeth," Ocean Eng. **172**, 562–574 (2019).
[21]G. Whitehouse, A. Sharma, and J. Keller, *Establishing Fluid Dynamics Scales Critical to Dynamic Interface Applications and Their Impact on Handling Qualities* (Office of Naval Research, 2021).
[22]N. Fernandez, N. Watson, I. Owen, and M. White, "A comparative assessment of the NATO-GD and SFS2 ship airwakes and their influence upon helicopter aerodynamic loading," in *Proceedings of the Vertical Flight Society 78th Annual Forum* (The Vertical Flight Society, 2022).
[23]J. Counihan, "Adiabatic atmospheric boundary layers: A review and analysis of data from the period 1880–1972," Atmos. Environ. **9**(10), 871–905 (1975).
[24]N. Rosenfeld, K. Kimmel, and A. J. Sydney, "Investigation of ship topside modeling practices for wind tunnel experiments," AIAA Paper No. 2015-0245, 2015.
[25]N. J. Cook, "The Deaves and Harris ABL model applied to heterogeneous terrain," J. Wind Eng. Ind. Aerodyn. **66**(3), 197–214 (1997).
[26]S. S. Cook, "Effects of headwinds on towing tank resistance and PMM tests for ONR tumblehome," M.Sc. thesis (University of Iowa, 2011).
[27]B. K. Kıyak, S. Sarı, A. Doğrul, and S. Bayraktar, "Airwake control of ONR tumblehome using CVG," J Naval Sci. Eng. **22**, 189–216 (2026).
[28]S. Sarı, A. Dogrul, and S. Bayraktar, "The aerodynamic wind loads of a naval surface combatant In model scale," in *New Technologies, Development and Application V* (Springer, Sarajevo, Bosnia and Herzegovina, 2022), pp. 68–76.
[29]D. Seth, Z. Zhang, E. P. Gnanamanickam, and J. G. Leishman, "Time-resolved PIV measurements of a ship airwake in a simulated atmospheric boundary layer," AIAA Paper No. 2020-2071, 2020.
[30]J. W. Cooley and J. W. Tukey, "An algorithm for the machine calculation of complex Fourier series," Math. Comput. **19**(90), 297–301 (1965).
[31]P. Welch, "The use of fast Fourier transform for the estimation of power spectra: A method based on time averaging over short, modified periodograms," IEEE Trans. Audio Electroacoust. **15**(2), 70–73 (1967).
[32]J. S. Bendat and A. G. Piersol, *Random Data: Analysis and Measurement Procedures*, 4th ed. (John Wiley & Sons, 2010).
[33]M. Farge, "Wavelet transforms and their applications to turbulence," Annu. Rev. Fluid Mech. **24**, 395–458 (1992).
[34]M. Farge, N. Kevlahan, V. Perrier, and E. Goirand, "Wavelets and turbulence," Proc. IEEE **84**(4), 639–669 (1996).
[35]C. Torrence and G. P. Compo, "A practical guide to wavelet analysis," Bull. Am. Meteorol. Soc. **79**(1), 61–78 (1998).
[36]H. K. Versteeg and W. Malalasekera, *An Introduction to Computational Fluid Dynamics: The Finite Volume Method* (Pearson Education Limited, 2007).
[37]Safety Regulation Group, *Offshore Helideck Environmental Research* (UK Civil Aviation Authority, 2008).
[38]Safety Regulation Group, *Standards for Offshore Helicopter Landing Areas* (UK Civil Aviation Authority, 2023).
[39]J. Bludau, "Real-Time simulation of the Ship-Rotorcraft dynamic interface using local recalculation with the Lattice-Boltzmann method," Ph.D. thesis (Munich Technical University, 2024).
[40]A. Zanoni, P. Garbo, and G. Quaranta, "Online evaluation of helicopter pilot workload during flight simulator experiments," AIAA Paper No. 2022-0511, 2021.
[41]N. Matayoshi, J. S. Forrest, S. J. Hodge, G. D. Padfield, and I. Owen, "Relationship between pilot workload and turbulence intensity for helicopter operations in harsh environments," in *Annual Forum Proceedings* (AHS International, Grapevine, TX, 2009), pp. 1595–1603.

18 November 2026 10:48:16

Published under an exclusive license by AIP Publishing